Increasing the high rate performance of mixed metal phospho-olivine cathodes through collective and cooperative strategies

Bo Ding [a], Ge Ji [b], Yue Ma [a], Pengfei Xiao [b], Li Lu [b], Jim Yang Lee [a,*]
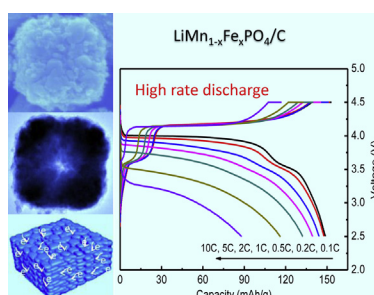
[a] NUS Graduate School for Integrative Sciences and Engineering (NGS), Center for Life Sciences (CeLS), #05-01 28 Medical Drive, Singapore 117456, Singapore
[b] Department of Mechanical Engineering, National University of Singapore, 9 Engineering Drive 1, Singapore 117576, Singapore

HIGHLIGHTS

- A monodisperse $LiMn_{1-x}Fe_xPO_4/C$ cathode with bi-continuous networks for electron and Li^+ transport.
- Aliovalent doping, carbon coating and mesoscale assembly were used in tandem to optimize performance.
- Excellent electrochemical performance for reversible Li^+ storage (116 mAh g^{-1} at 5 C, 88 mAh g^{-1} at 10 C).

GRAPHICAL ABSTRACT

ARTICLE INFO

ABSTRACT

The performance of lithium manganese phosphate as a lithium-ion battery cathode material is improved by collective and cooperative strategies including Fe substitution, carbon coating, and the assembly of carbon-coated $LiMn_{1-x}Fe_xPO_4$ nanocrystals into a highly dense packing of monodisperse microboxes. These strategies are implemented experimentally by a facile and scalable synthesis method. The dense packing allows the conductive carbon coating to be interconnected into a continuous three-dimensional network for electron conduction. The porosity in the packed structure forms the complementary network for Li^+ transport in the electrolyte. The primary particles are nanosized and Fe-substituted to improve the effectiveness of Li^+ insertion and extraction reactions in the solid phase. The reduction of transport resistance external and internal to the nanocrystals yields a Li storage host with good rate performance (116 mAh g^{-1} at 5 C discharge rate where $C = 170$ mA g^{-1}) and cycle stability (95% retention of initial capacity in 50 cycles). Electrochemical impedance spectroscopy and morphology examination of the cycled microboxes reveal a robust packed structure with stable surfaces.

© 2013 Elsevier B.V. All rights reserved.

1. Introduction

The relentless efforts in using particle size reduction, conductive surface coating, and mesoscale assembly to improve the performance of $LiFePO_4$ have resulted in a material very different from when it was first introduced [1–6]. $LiFePO_4$ is now considered as a safe cathode material with good cycle life and reasonable cost for large format lithium ion batteries [2,3,7,8]. Isostructural with $LiFePO_4$, $LiMnPO_4$ offers 20% more energy density because of a voltage plateau which is 0.7 V higher than that of $LiFePO_4$ [9]. Similar to the early days of $LiFePO_4$, the development of $LiMnPO_4$ is impeded by its extremely low electronic and ionic conductivities [10,11]. Taking a lesson from $LiFePO_4$, aliovalent doping, crystal size reduction, and carbon painting have been applied to $LiMnPO_4$ to

* Corresponding author. Department of Chemical and Biomolecular Engineering, National University of Singapore, 10 Kent Ridge Crescent, Singapore 119260, Singapore. Tel.: +65 6516 2899; fax: +65 67791936.
E-mail address: cheleejy@nus.edu.sg (J.Y. Lee).

increase intrinsic electronic conductivity, shorten the Li^+ diffusion path length in the nanocrystal, and reduce the external electrical resistance respectively. Success has thus far been limited. The highly insulating nature of $LiMnPO_4$, and the JahnTeller distortion of Mn^{3+} ions where the mismatch between $LiMnPO_4$ and $MnPO_4$ phases repel Li^+ diffusion, [12] thereby requiring more extreme nanocrystal size reduction (to 10 nm and below) to ameliorate the transport limitations in the solid phase. A large amount of carbon is also required for encapsulating the nanocrystal surface when sub-10 nm nanocrystals are used [13]. The use of small nanocrystals and excess carbon would however lower the overall energy density of the cathode material substantially [14].

Recent studies have shown that the partial substitution of Mn with Fe can form $LiMn_{1−x}Fe_xPO_4$ (x from 0 to 1) solid solutions with higher electronic and ionic conductivities and less Jahn−Teller distortion [12,15−18], allowing the same level of performance in nanocrystals larger than those of $LiMnPO_4$ (sub-100 vs sub-10 nm) [16,19]. Good rate performance in practice, however, still uses an excessive amount of carbon for the electrical connection of discrete nanocrystals. Overall energy density and power density of the cathode therefore remain to be low. The assembly of discrete primary nanocrystals into compact organized aggregates offers an opportunity to improve the volumetric energy and power densities while keeping the nanocrystal advantage [20,21]. The assembly has to be implemented in such a way that it possesses co-continuous electronic and ionic conductive networks for the transport of electrons and Li^+ [22−24]. Since electron transport between the particles in the aggregates depends on in-situ formed thin carbon films where electrical conductivity may be limited, the aggregate size has to be moderate so as not to incur transport limitations at the aggregate level [25]. Thus mesoscale assembly is preferred over macroscale assembly. Due to the difficulty in synthesizing uniformly sized $LiMn_{1−x}Fe_xPO_4$ nanocrystals, and the assembly of nanocrystals into mesoscale structures, there have been very few reports on assembled $LiMn_{1−x}Fe_xPO_4$ structures in the literature. Hence the development of facile and scalable methods for the synthesis and assembly of $LiMn_{1−x}Fe_xPO_4$ nanocrystals into compact mesoscale structures with co-continuous networks for electron and ion conduction is essential for realizing the true potential of $LiMnPO_4$-based cathodes.

This is a report of design of co-continuous phase-pure monodisperse $LiMn_{1−x}Fe_xPO_4$/C microboxes through collective and cooperative strategies and their preparation. The microboxes were constituted from densely packed carbon-coated 100−200 nm $LiMn_{1−x}Fe_xPO_4$ nanocrystals. Pores were formed by the interstices in the packed structure. A small amount of Fe substitution was used to improve the intrinsic electrochemical properties of $LiMnPO_4$ [26]. Each nanocrystal was coated with a layer of carbon to reduce the electrical resistance between the nanocrystals. The nanocrystals in the microboxes were densely packed so that the carbon coating formed a continuous 3D network for electron conduction through the aggregates. The interstices in the microboxes formed the complementary network of interconnected pores to support efficient electrolyte infusion to reduce the Li^+ diffusion resistance external to the nanocrystals. Monodispersity of the microboxes also enabled a more even charge distribution and minimized the local perturbations of mass transfer processes. Consequently these monodisperse microboxes were capable of delivering excellent discharge capacities of 116 mAh g^{-1} at the 5 C rate (C = 170 mA g^{-1}) and 88 mAh g^{-1} at the 10 C rate. Such impressive rate performance places these microboxes the best of $LiMnPO_4$-based cathodes with low carbon loading. The preparation leveraged firstly on a high yield synthesis of monodisperse $Mn_{1−x}Fe_xPO_4·H_2O$ microboxes (>95% yield) by probe sonication assisted precipitation. A solution chemistry method that preserved the size and shape of the

microboxes was then applied to implant the carbon source; followed by a finishing heat treatment.

2. Experimental section

2.1. Materials preparation

The synthesis of monodisperse $LiMn_{1−x}Fe_xPO_4$/C microboxes was a two-step process. Monodisperse $Mn_{1−x}Fe_xPO_4·H_2O$ microboxes were fabricated first; followed by reactions with lithium acetate and glucose monohydrate in ethanol and heat treatment.

Monodisperse $Mn_{1−x}Fe_xPO_4·H_2O$ microboxes were prepared by the co-precipitation method. 4.25 g $Mn(NO_3)_2·4H_2O$ (Sigma Aldrich) and 1.07 g $Fe(NO_3)_3·9H_2O$ (Sigma Aldrich) were dissolved in ethanol to a total volume of 30 ml, 5 ml H_3PO_4 (85 wt.%) (Mallinckrodt) was then added quickly under probe sonication (Sonics VCX 750 W) for 1 min. The resultant solution was transferred to a 50 ml Teflon-lined autoclave for 1 h of reaction at 40 °C. The reaction product was recovered as a precipitate, washed twice with DI water and centrifuged, and dried at 60 °C for 12 h. The progress in microbox formation was sampled by analysing the reaction mixture at 15 min, 30 min, 40 min, 1 h and 4 h into the reaction.

The synthesis of $LiMn_{1−x}Fe_xPO_4$/C was then carried out as follows: equimolar quantities of $LiCH_3COO·2H_2O$ (Sigma Aldrich) and $Mn_{1−x}Fe_xPO_4·H_2O$; and 30 wt.% glucose monohydrate were mixed in ethanol and bath-sonicated for 1 h (Branson 2510). Ethanol was then allowed to evaporate and the residue was calcined at 600 °C in flowing Ar for 12 h in a tube furnace. For comparison a sample, SSR-nano was also prepared by the solid-state reaction from a mixture of $LiCH_3COO·2H_2O$, $FeC_2O_4·2H_2O$ (Sigma Aldrich), $Mn(CH_3COO)_2·4H_2O$, $NH_4H_2PO_4$ (Sigma Aldrich) (Li:Fe:Mn:P = 1:0.13:0.87:1) and Super P carbon (10 wt.% of the final product). The mixture was ball-milled intermittently for a total of 4 h (30 min grinding followed by 30 min of rest). The mixture was heat-treated at 350 °C for 10 h, mixed with 10 wt.% sucrose and ball-milled again for one more hour before another heat-treatment at 600 °C for 12 h in flowing Ar.

2.2. Materials characterization

The morphologies of $LiMn_{1−x}Fe_xPO_4$/C microboxes and SSR-nano were examined by FESEM on a JEOL JSM-6700F; and by FETEM on a JEOL JEM-2010F. The carbon content in $LiMn_{1−x}Fe_xPO_4$/C was assayed by TGA on a Shimadzu DT-60H. Crystal structure determinations were based on X-ray diffraction measurements of the samples on a Bruker D8 Advance diffractometer using Cu Kα irradiation. EDX measurements were performed during the FESEM and FETEM sessions to obtain average elemental compositions and the compositions of single microboxes respectively.

2.3. Electrochemical measurements

Monodisperse $LiMn_{1−x}Fe_xPO_4$/C microboxes or SSR-nano (∼50 nm), Super P carbon and polyvinylidene fluoride (PVDF) (Sigma Aldrich) in a weight ratio of 8:1:1 were mixed into a consistent slurry in N-methylpyrrolidone (NMP) (Sigma Aldrich). The slurry was applied uniformly on an aluminium foil current collector to a loading of ∼3 mg cm^{-2} followed by drying in vacuum at 120 °C overnight. The thickness of the finished electrodes (after compression at 2 ton pressure) was 12 μm for the microboxes and 20 μm for SSR-nano. Electrode density, on the other hand, was 2.5 g cm^{-3} for the former and 1.5 g cm^{-3} for the latter. The difference in electrode thickness was due to the difference in material packing density. The working electrode, a lithium foil counter cum reference electrode, and a Celgard 2400 membrane separator were
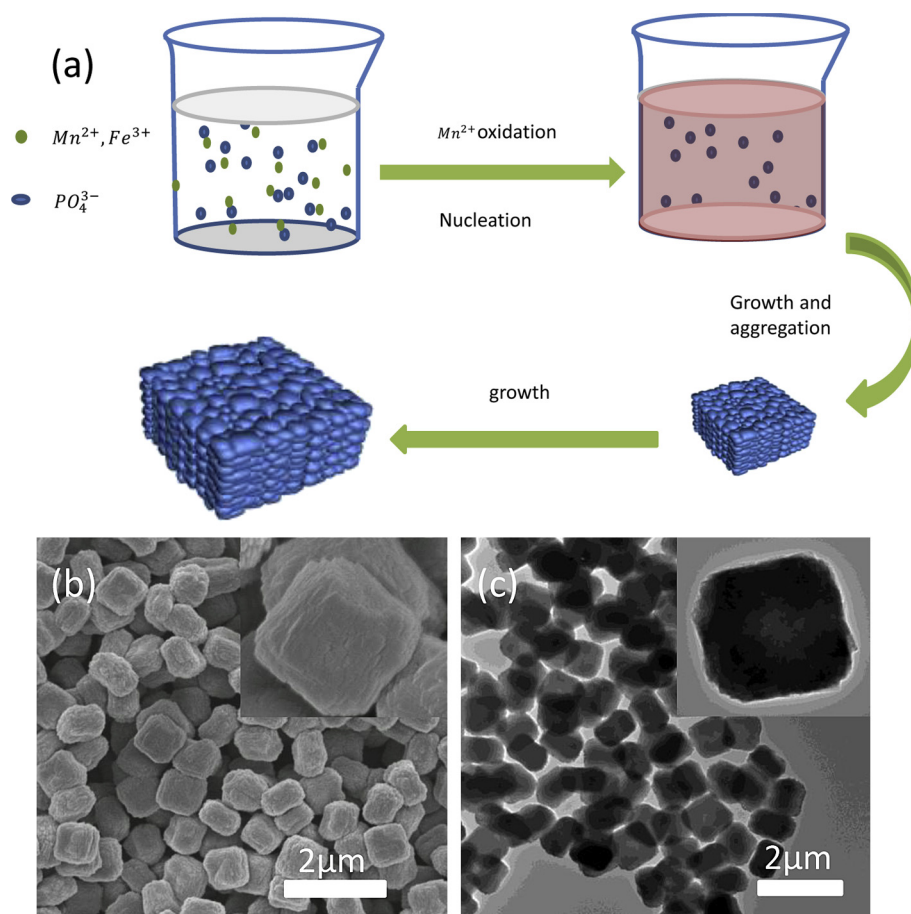
Fig. 1. (a) Schematic showing the preparative steps in the formation of $Mn_{1-x}Fe_xPO_4 \cdot H_2O$ microboxes; (b) SEM and (c) TEM images of the monodisperse $Mn_{1-x}Fe_xPO_4 \cdot H_2O$ microboxes with insets showing an individual microbox.
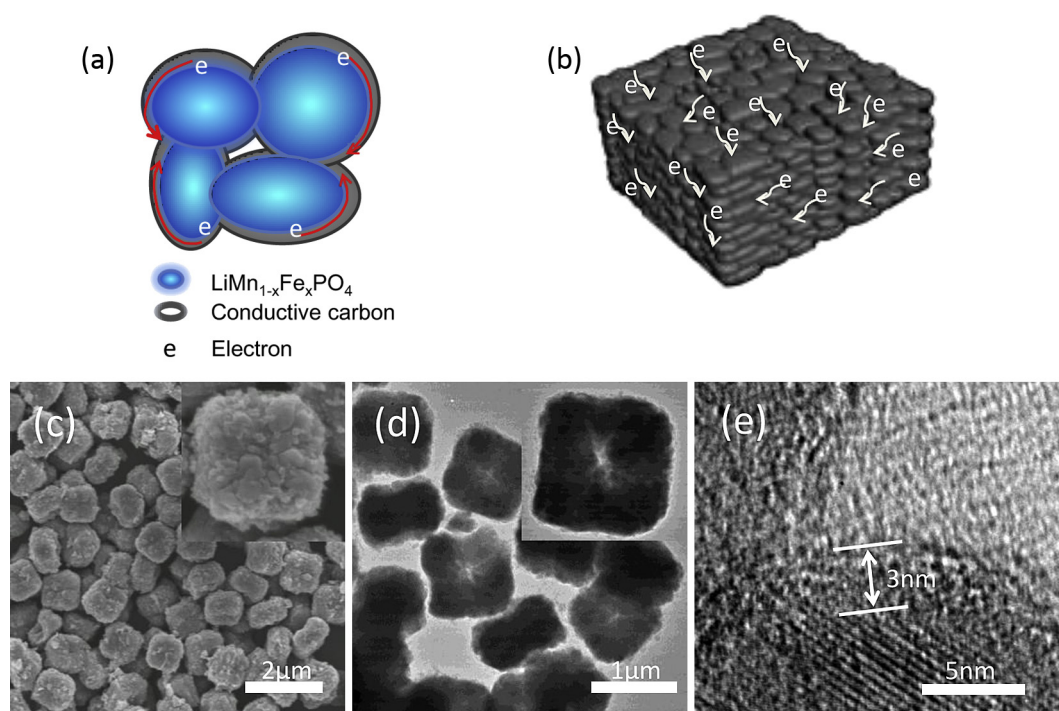

Fig. 2. (a) The interconnected carbon coating on $LiMn_{1-x}Fe_xPO_4/C$ nanocrystals and (b) 3D network for electron transport in carbon-coated microbox; (c) SEM and (d) TEM images of monodisperse $LiMn_{1-x}Fe_xPO_4/C$ microboxes; (e) HRTEM image showing a thin layer of disordered carbon on the nanocrystal surface.

assembled into a Swagelok cell. The electrolyte was 1 M $LiPF_6$ in a 1:1:1 (volume ratio) mixture of ethylene carbonate (EC), dimethyl carbonate (DMC) and diethyl carbonate (DEC) (Hohsen corp). The cells fabricated as such were tested on a Neware BTS-5V-1 mA battery tester. For the evaluation of rate capability, a constant-current constant-voltage (CC-CV) protocol was used where the cells were first charged galvanostatically at the 0.1 C rate from 2.5 V to 4.5 V followed by constant-voltage charging at 4.5 V until the current density decreased to 0.02 C. On the other hand, the cells were allowed to discharge at different constant-current densities. For the test of cycle stability, the cells were first cycled at 0.1 C for 5 cycles, followed by charging at 0.2 C and then discharging at 0.5 C. An Autolab µAUTOLAB potentiostat/galvanostat electrochemical workstation was used for CV at 0.05 mV s^{-1}. EIS in the frequency range 100 kHz to 0.1 Hz was also performed on the same workstation using a FRA2 type III attachment.

3. Results and discussion

3.1. Monodisperse Mn$_{1-x}$Fe$_x$PO$_4$·H$_2$O microboxes

Mn$_{1-x}$Fe$_x$PO$_4$·H$_2$O was formed by the classical La Mer's burst nucleation and growth mechanism illustrated in Fig. 1a [5]. In brief, after the addition of H_3PO_4 to a mixture of Mn^{2+} and Fe^{3+} in ethanol, Mn^{2+} was oxidized by NO_3^- in the presence of H^+ [27]. The process was fast; allowing Mn^{3+} to accumulate rapidly within a short period of time. Burse nucleation occurred when the solubility of the mixed phosphate Mn$_{1-x}$Fe$_x$PO$_4$·H$_2$O exceeded its supersaturation limit in the solution. The nuclei grew into nanoparticles following the crystal habit of Mn$_{1-x}$Fe$_x$PO$_4$·H$_2$O. It should be emphasized that no surfactant was used in the synthesis, and naturally the nanoparticles aggregated to reduce their surface energy. Scanning electron microscopy (SEM) (Fig. 1b) and transmission electron microscopy (TEM) (Fig. 1c) images of Mn$_{1-x}$Fe$_x$PO$_4$·H$_2$O synthesized as such show box-like aggregates ∼1 µm in length and width and 600 nm in height with very high monodispersity. Closer examinations revealed that the microboxes consisted of closely stacked plate-like nanocrystals (See Fig. S1). There were small crevices in the packing (Inset of Fig. 1c) where small molecules such as glucose could go through. There were no further shape changes after the microboxes were formed (in 20 min). Increase in time in the first hour of reaction only increased the size of the microboxes. A longer reaction time, however, detected the onset of Oswald ripening where the redistribution of primary particles resulted in some loss of aggregate monodispersity (See Fig. S2 for a reaction time of 4 h). Fig. S3 shows that rapid addition of H_3PO_4 and ultrasound irradiation was necessary to provide the uniform reaction environment for fast nucleation and homogeneous aggregate growth. X-ray diffraction (XRD) analysis of the microboxes yielded the diffraction peaks of Mn$_{1-x}$Fe$_x$PO$_4$·H$_2$O (Fig. S4, JCPDS No. 78-1082). Energy dispersive x-ray (EDX) measured a Mn:Fe elemental ratio of 6.65:1 for the microboxes (Fig. S5). This value was used to derive the molecular formula of Mn$_{0.87}$Fe$_{0.13}$PO$_4$·H$_2$O. The Mn content in Mn$_{0.87}$Fe$_{0.13}$PO$_4$·H$_2$O was sufficiently high to support an extended operation in the 4 V region to reap the benefit of increased energy density.

3.2. Monodisperse LiMn$_{1-x}$Fe$_x$PO$_4$/C microboxes

Fig. 2a and b are schematics of the surface carbon coating emphasizing on its connectivity to form a continuous 3D network which electrically integrated the nanocrystals. Fig. 2c and d show that the incorporation of lithium into the Mn$_{1-x}$Fe$_x$PO$_4$·H$_2$O precursor to form LiMn$_{1-x}$Fe$_x$PO$_4$ did not change the size and shape of the microboxes. This was because the incorporation of Li$^+$

accompanied by the departure of H_2O from Mn$_{1-x}$Fe$_x$PO$_4$·H$_2$O and the reduction of M^{3+} (M = Mn, Fe) by glucose decomposition, did not involve major structural rearrangement [27,28]. Hence the LiMn$_{1-x}$Fe$_x$PO$_4$ synthesized as such was well poised to retain the monodispersity and the geometrical features of the Mn$_{1-x}$Fe$_x$PO$_4$·H$_2$O microboxes. There was, however, some increase in surface roughness after lithium incorporation. The structure and monodispersity of the microboxes were however not significantly affected by the ensuing heat treatment. Monodispersity is desirable as the transport resistances (both electronic and ionic) can be more evenly distributed to support higher rate performance and cycle stability in battery operations.

Ultrasonication was critical in this step to promote the extensive penetration of glucose molecules into the densely packed Mn$_{1-x}$Fe$_x$PO$_4$·H$_2$O microbox structure. The carbon layer formed by the ensuing carbonization of adsorbed glucose on the nanocrystal surface was effective in suppressing the crystal growth of the primary particles; thereby preserving the size of the primary particles during heat treatment. Consequently the microboxes still consisted of stacked 100−200 nm nanocrystals after the heat treatment (See Fig. S6). Nonetheless some thermally induced ripening had occurred to result in more distinctive boundaries between the
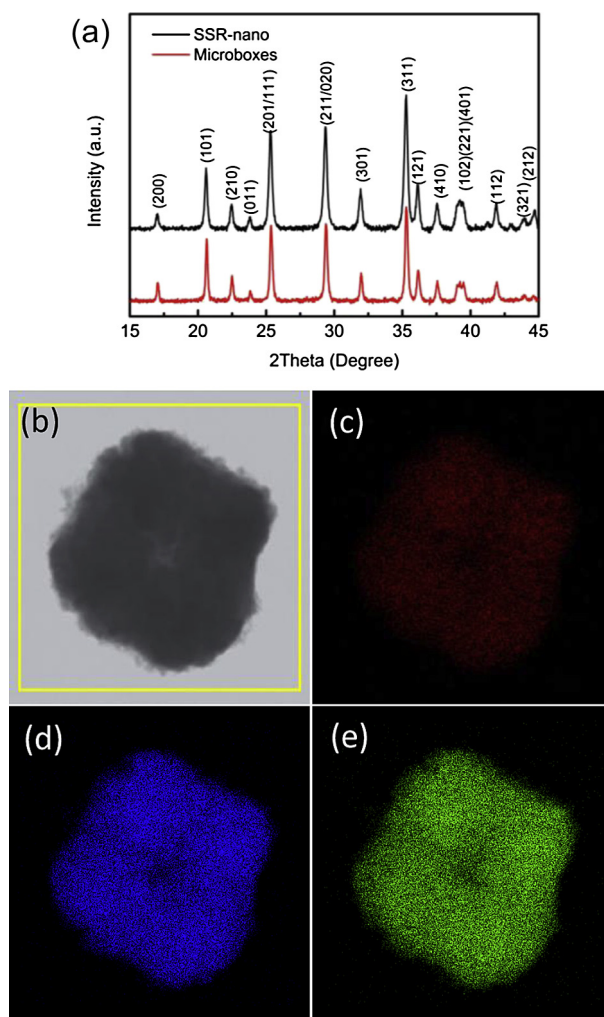

Fig. 3. (a) XRD patterns of the microboxes and SSR-nano; (b−e) TEM image of a single microbox and corresponding element mapping, Fe (red), Mn (blue) and P (green). (For interpretation of the references to colour in this figure legend, the reader is referred to the web version of this article.)

nanocrystals and some hollowing of the microbox core area (Fig. 2c and d insets). The increase in the porosity of the microboxes due to these internal features could indeed be beneficial to electrolyte permeation during battery operations. Porosity also contributed to structural stability by providing free surfaces to reduce the microstrain in repeated charging and discharging. The porosity increase was however moderate so as not to undermine the mechanical strength of the structure. Fig. 2e shows that the carbon coating on the nanocrystals was ~3 nm thick. Thermal gravimetric analysis (TGA) measured the total carbon content in the microboxes to be 5.93 wt.% (Fig. S7). For comparison, the LiMn$_{1-x}$Fe$_x$PO$_4$/C (SSR-nano) prepared via the solid-state synthesis route consisted only of unorganized 50–100 nm particles (Fig. S8).

XRD data in the 2 theta range of 15–45° as shown in Fig. 3a confirmed the ordered olivine structure (space group: Pnma) of LiMn$_{1-x}$Fe$_x$PO$_4$/C microboxes and SSR-nano. There were no peaks that could be attributed to LiFePO$_4$ and LiMnPO$_4$ phases; indicating the effectiveness of the syntheses in producing phase-pure Fe-substituted LiMn$_{1-x}$Fe$_x$PO$_4$ solid solutions. The absence of impurities such as Fe$_2$O$_3$, Li$_3$(Fe,Mn)$_2$(PO$_4$)$_3$ in the olivine structure, which are known to impair the performance in reversible Li$^+$ storage, suggests the effective reduction of Mn^{3+} and Fe^{3+} to Mn^{2+} and Fe^{2+} by glucose respectively [29–31]. The uniformity of Fe and Mn distributions in the microboxes was confirmed by elemental mapping (Fig. 3b–e), and indicated the successful partial substitution of Mn by Fe in the olivine structure. The distributive substitution of Mn by Fe in LiMnPO$_4$ could restrain Jahn–Teller distortion to reduce the electron hopping energy barrier and the distortion of the Li$^+$ transport channels. The electrochemical activity of olivine was expected to improve as a result [12]. The high Mn content of the monodisperse microboxes ($x = 0.13$ in LiMn$_{1-x}$Fe$_x$PO$_4$/C) increased the use of the 4.1 V voltage plateau and decreased the 3.5 V region caused by the Fe^{2+}/Fe^{3+} redox reaction.

3.3. Electrochemical performance and structure stability of LiMn$_{1-x}$Fe$_x$PO$_4$/C microboxes

Fig. 4a shows the typical charge and discharge curves of the microboxes and SSR-nano at the 0.1 C rate. The microboxes clearly outperformed SSR-nano in terms of gravimetric Li$^+$ storage capacity and energy density. The discharge capacity of LiMn$_{1-x}$Fe$_x$PO$_4$/C microboxes was 148 mAh g^{-1} with a distinct voltage plateau at 4.1 V characteristic of the two-phase Mn$^{2+/3+}$ redox reaction and a sloping discharge curve centring at 3.6 V corresponding to the single-phase Fe$^{2+/3+}$ redox reaction. The well-defined voltage plateau is an indication of good electrical connectivity between the nanocrystals in the aggregates [32,33]. By comparison SSR-nano only delivered 110 mAh g^{-1} on discharge and displayed a narrow discharge plateau at 3.8 V for the Mn$^{2+/3+}$ redox reaction suggesting a poorer material electrical conductivity. Even with the use of a large excess of conductive carbon additive in electrode fabrication, SSR-nano still exhibited substantial interparticle contact resistance indicating inadequate electronic integration of its nanocrystals. The corollary from these observations is that only the monodisperse microboxes embodied an effective network for electron transport between the nanocrystals. The
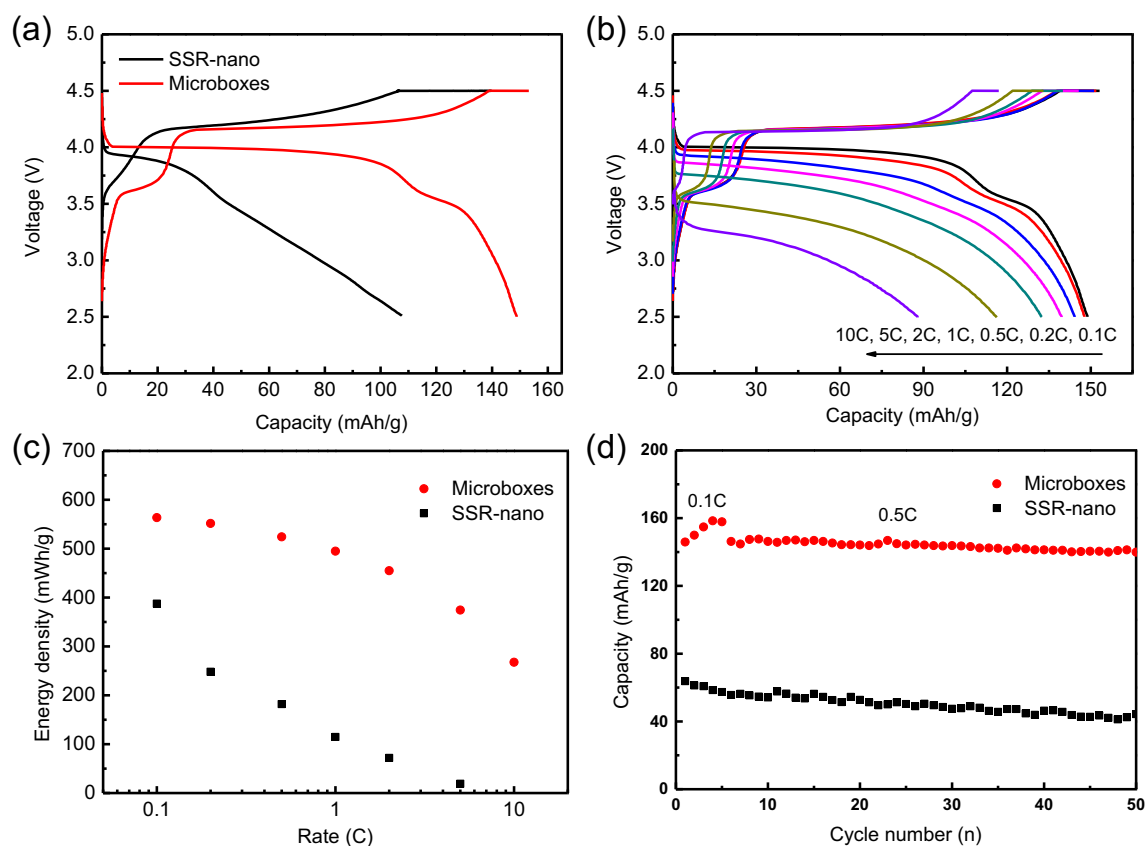

Fig. 4. (a) Charge and discharge curves at 0.1 C of monodisperse LiMn$_{1-x}$Fe$_x$PO$_4$/C microboxes and SSR-nano. Cells were charged by the constant current-constant voltage (CC-CV) protocol from 2.5 V to 4.5 V at 0.1 C and then rested at 4.5 V until the current density decreased to 0.02 C; (b) rate performance of the monodisperse microboxes, same charge protocol as that in (a) but the discharge was carried out at different rates; (c) energy density *vs* C-rate plot; (d) cycling performance at 0.5 C (Charging protocol: CC-CV, 0.2 C charging, holding at 4.5 V until 0.05 C).
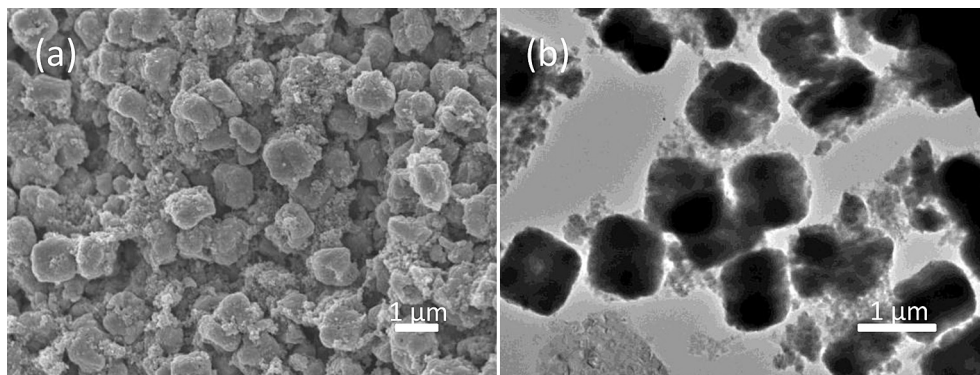
Fig. 5. (a) SEM and (b) TEM images of the cycled microboxes electrode.

redox reactions were also characterized by cyclic voltammetry (CV) at a slow scan rate of 0.05 mV s^{-1} (Fig. S9). The resulting voltammograms showed an anodic peak at 3.67 V and a cathodic peak at 3.53 V due to the oxidation of Fe^{2+} and the reduction of Fe^{3+} respectively. Likewise the peaks at 4.21 V and 3.88 V could be attributed to the oxidation Mn^{2+} and the reduction of Mn^{3+} respectively. The Mn^{3+} reduction peak (Li^+ intercalation) was sharper and more distinct than the Mn^{2+} oxidation peak (Li^+ de-intercalation) suggesting that discharging was kinetically more facile than charging. We could surmise two possible reasons for the asymmetry in kinetic behaviour: stronger Li^+–Mn^{2+} attractive interaction during discharge and weaker V_{Li+}–Mn^{3+}, V_{Li+}–Fe^{3+} attractive interactions during charging at the 4 V regions. Another hypothesis is the narrowing of the Li^+ diffusion channel during charging thereby increasing the difficulty in continuous Li^+ extraction.

The monodisperse microboxes also delivered very good high rate performance. Fig. 4b shows the measurements carried out at different discharge rates from 0.1 C to 10 C. The monodisperse microboxes were able to deliver discharge capacities of 116 mAh g^{-1} and 88 mAh g^{-1} at rates as high as 5 C (850 mA g^{-1}) and 10 C (1700 mA g^{-1}) respectively, even though their primary particle size was large compared with previously reported LiMn$_{1-x}$Fe$_x$PO$_4$/C (120 mAh g^{-1} at 2 C, C = 170 mA g^{-1}, with 30 wt.% carbon in the composite) [16]. Voltage plateaus were still evident at the 10 C rate, reflecting the superior electronic properties of the microboxes relative to unorganized nanocrystals. In terms of gravimetric energy density (Fig. 4c), the microboxes showed no appreciable decrease in energy density until the discharge rate was 2 C and above. By comparison, SSR-nano showed substantially lower energy densities throughout the range of tested current densities. The persistence of high energy density was made possible by an effective network of electron and Li^+ transport which minimized polarizations due to transport limitations.

Other than a high rate performance, the microboxes were also stable to cycling. Fig. 4d shows that after 5 conditioning cycles at low rates, the microboxes retained ~96% of its initial discharge capacity at 0.5 C for a total of 50 cycles. By comparison the SSR-nano, which had lower capacity at 0.5 C, provided only 40 mAh g^{-1}, or approximately one third of the capacity of the microboxes, in the same number of cycles. The microboxes were also able to maintain distinct voltage profiles when charging at the 0.2 C rate and discharging at the 0.5 C rate (Fig. S10). The microboxes after different numbers of cycles were analysed by electrochemical impedance spectroscopy (EIS) for additional information on material cyclability. The data in Fig. S11 was collected from a cell cycled under the same condition as that of Fig. 4d. EIS measurements were performed under the open circuit condition after the 10th and the 50th cycles. The increase in the size of the semi-circular arc relative to a pristine, un-cycled electrode could be attributed to the formation of a solid electrolyte interphase (SEI) on the surface of the microboxes [34–36]. The size of the semi-circular arc changed very little after 10 cycles, indicating the stability and the robustness of the SEI layer. The Swagelok cell was disassembled after 50 cycles. The electrode film was removed from the aluminium current collector and washed with NMP for morphology examination. Fig. 5 shows that many of the microboxes after cycling kept the same box-like appearance and similar nanocrystal size and pore structure as those before cycling. Considering the ~ 10% of volume change during charging and discharging, the microboxes were therefore chemically and mechanically resilient [37]. Structural stability was critical to preserving the integrity of the conducting network in repetitive charge and discharge operations for a stable cycling performance. Monodispersity of the microboxes was an important feature since each microbox was subjected to similar conditions in electron and Li^+ transfers. Consequently a more macroscopically uniform current distribution could be maintained in the electrode. Such uniformity minimized local perturbations to contribute to a more sustained cycling performance [38–40].

4. Conclusions

In brief, we have synthesized a high performance LiMn$_{1-x}$Fe$_x$PO$_4$/C based on a combination of several materials design strategies to improve a number of performance areas. The composite, in the form of monodisperse LiMn$_{1-x}$Fe$_x$PO$_4$/C microboxes, was prepared by a facile and scalable synthesis method. It represents the best LiMn$_{1-x}$Fe$_x$PO$_4$/C-based cathodes and delivered high energy density with excellent rate capability and cycling stability. The very satisfactory electrochemical performance could be attributed to a compact porous microstructure with a 3D electron and ionic conductive network for efficient electron and mass transport. Macroscopically size and shape uniformity supported a more uniform current distribution in the electrode, and together with a resilient microstructure and stable interface, contributed to the high cycle stability. The synthesis method can be easily scaled up for volume production and hence these microboxes are more than a laboratory curiosity.

Acknowledgements

Appendix A. Supplementary data

Supplementary data related to this article can be found at http://dx.doi.org/10.1016/j.jpowsour.2013.08.114.

References

[1] A.K. Padhi, K.S. Nanjundaswamy, J.B. Goodenough, J. Electrochem. Soc. 144 (1997) 1188–1194.
[2] Y.G. Wang, Y.R. Wang, E.J. Hosono, K.X. Wang, H.S. Zhou, Angew. Chem. Int. Ed. 47 (2008) 7461–7465.
[3] G.X. Wang, H. Liu, J. Liu, S.Z. Qiao, G.Q.M. Lu, P. Munroe, H. Ahn, Adv. Mater. 22 (2010) 4944–4948.
[4] Z.H. Li, D.M. Zhang, F.X. Yang, J. Mater. Sci. 44 (2009) 2435–2443.
[5] C.W. Sun, S. Rajasekhara, J.B. Goodenough, F. Zhou, J. Am. Chem. Soc. 133 (2011) 2132–2135.
[6] B. Ellis, P. Subramanya Herle, Y.H. Rho, L.F. Nazar, R. Dunlap, L.K. Perry, D.H. Ryan, Faraday Discuss. 134 (2007) 119–141.
[7] K. Dokko, S. Koizumi, K. Sharaishi, K. Kanamura, J. Power Sources 165 (2007) 656–659.
[8] H. Nakano, K. Dokko, S. Koizumi, H. Tannai, K. Kanamura, J. Electrochem. Soc. 155 (2008) A909–A914.
[9] D. Choi, D. Wang, I.-T. Bae, J. Xiao, Z. Nie, W. Wang, V.V. Viswanathan, Y.J. Lee, J.-G. Zhang, G.L. Graff, Z. Yang, J. Liu, Nano Lett. 10 (2010) 2799–2805.
[10] S.K. Martha, B. Markovsky, J. Grinblat, Y. Gofer, O. Haik, E. Zinigrad, D. Aurbach, D. Drezen, D. Wang, G. Deghenghi, I. Exnar, J. Electrochem. Soc. 156 (2009) A541–A552.
[11] P.R. Kumar, M. Venkateswarlu, M. Misra, A.K. Mohanty, N. Satyanarayana, J. Electrochem. Soc. 158 (2011) A227–A230.
[12] S.P. Ong, V.L. Chevrier, G. Ceder, Phys. Rev. B. 83 (2011) 1–7.
[13] H. Yoo, M. Jo, B.S. Jin, H.S. Kim, J. Cho, Adv. Energy Mater. 1 (2011) 347–351.
[14] V. Etacheri, R. Marom, R. Elazari, G. Salitra, D. Aurbach, Energy Environ. Sci. 4 (2011) 3243–3262.
[15] S.K. Martha, J. Grinblat, O. Haik, E. Zinigrad, T. Drezen, J.H. Miners, I. Exnar, A. Kay, B. Markovsky, D. Aurbach, Angew. Chem. Int. Ed. 48 (2009) 8559–8563.
[16] S.M. Oh, H.G. Jung, C.S. Yoon, S.T. Myung, Z.H. Chen, K. Amine, Y.K. Sun, J. Power Sources 196 (2011) 6924–6928.
[17] S.M. Oh, S.T. Myung, J.B. Park, B. Scrosati, K. Amine, Y.K. Sun, Angew. Chem. Int. Ed. 51 (2012) 1853–1856.
[18] H.L. Wang, Y. Yang, Y.Y. Liang, L.F. Cui, H.S. Casalongue, Y.G. Li, G.S. Hong, Y. Cui, H.J. Dai, Angew. Chem. Int. Ed. 50 (2011) 7364–7368.
[19] A. Yamada, Y. Kudo, K.Y. Liu, J. Electrochem. Soc. 148 (2001) A1153–A1158.
[20] Y. Ma, G. Ji, B. Ding, J.Y. Lee, J. Mater. Chem. 22 (2012) 24380–24385.
[21] M. Gaberscek, J. Moskon, B. Erjavec, R. Dominko, J. Jamnik, Electrochem. Solid-State Lett. 11 (2008) A170–A174.
[22] X.W. Lou, Y. Wang, C. Yuan, J.Y. Lee, L.A. Archer, Adv. Mater. 18 (2006) 2325–2329.
[23] D. Chen, X. Mei, G. Ji, M. Lu, J. Xie, J. Lu, J.Y. Lee, Angew. Chem. Int. Ed. 51 (2012) 2409–2413.
[24] G. Ji, Y. Ma, B. Ding, J.Y. Lee, Chem. Mater. 24 (2012) 3329–3334.
[25] S. Dargaville, T.W. Farrell, J. Electrochem. Soc. 157 (2010) A830–A840.
[26] A. Yamada, Y. Takei, H. Koizumi, N. Sonoyama, R. Kanno, K. Itoh, M. Yonemura, T. Kamiyama, Chem. Mater. 18 (2006) 804–813.
[27] L. Wang, W.T. Sun, X.M. He, J.J. Li, C.Y. Jiang, Int. J. Electrochem. Sci. 6 (2011) 2022–2030.
[28] L. Wang, W.T. Sun, J.J. Li, J. Gao, X.M. He, C.Y. Jiang, Int. J. Electrochem. Sci. 7 (2012) 3591–3600.
[29] A. Ait Salah, A. Mauger, K. Zaghib, J.B. Goodenough, N. Ravet, M. Gauthier, F. Gendron, C.M. Julien, J. Electrochem. Soc. 153 (2006) A1692–A1701.
[30] K. Dokko, K. Shiraishi, K. Kanamura, J. Electrochem. Soc. 152 (2005) A2199–A2202.
[31] D.Y.W. Yu, K. Donoue, T. Kadohata, T. Murata, S. Matsuta, S. Fujitani, J. Electrochem. Soc. 155 (2008) A526–A530.
[32] R. Cornut, D. Lepage, S.B. Schougaard, J. Electrochem. Soc. 159 (2012) A822–A827.
[33] G.J. Nelson, B.N. Cassenti, A.A. Peracchio, W.K.S. Chiu, J. Electrochem. Soc. 159 (2012) A598–A603.
[34] D. Choi, J. Xiao, Y.J. Choi, J.S. Hardy, M. Vijayakumar, M.S. Bhuvaneswari, J. Liu, W. Xu, W. Wang, Z.G. Yang, G.L. Graff, J.G. Zhang, Energy Environ. Sci. 4 (2011) 4560–4566.
[35] Z. Bakenov, I. Taniguchi, J. Power Sources 195 (2010) 7445–7451.
[36] J. Hong, F. Wang, X. Wang, J. Graetz, J. Power Sources 196 (2011) 3659–3663.
[37] G. Li, H. Azuma, M. Tohda Electrochem, Solid-State Lett. 5 (2002) A135–A137.
[38] J.L. Li, B.L. Armstrong, J. Kiggans, C. Daniel, D.L. Wood, Langmuir 28 (2012) 3783–3790.
[39] C.-C. Li, X.-W. Peng, J.-T. Lee, F.-M. Wang, J. Electrochem. Soc. 157 (2010) A517–A520.
[40] W. Porcher, B. Lestriez, S. Jouanneau, D. Guyomard, J. Electrochem. Soc. 156 (2009) A133–A144.